











# The Phenomena Involved in the Thermal-dependent Tensile Mechanical Tests of *Premium* Rail Steel

João Vitor de Oliveira Cordeiro<sup>a,\*</sup> , Henrique Boschetti Pereira<sup>a</sup> ,  
Luiz Felipe Bauri<sup>a</sup> , André Luis Hansen Vieira<sup>a</sup> , Yuji Guilherme Iko Wasano<sup>a</sup>,  
Arthur Helfstein Moura<sup>a</sup> , Marcos Dorigão Manfrinato<sup>a,b</sup> , Edwan Anderson Ariza Echeverri<sup>c</sup> ,  
Luiz Henrique Dias Alves<sup>d</sup> , Giovanni Gonçalves Ribamar<sup>a</sup> , Hédio Goldenstein<sup>a</sup> 

<sup>a</sup>Universidade de São Paulo, Escola Politécnica, Departamento de Engenharia Metalúrgica e de Materiais, São Paulo, SP, Brasil.

<sup>b</sup>FATEC Sorocaba, Sorocaba, SP, Brasil.

<sup>c</sup>Universidad del Magdalena, Facultad de Ingeniería, Santa Marta, Colômbia.

<sup>d</sup>Universidade Federal de Juiz de Fora, Juiz de Fora, MG, Brasil.

Received: February 17, 2025; Revised: May 11, 2025; Accepted: May 29, 2025

This study investigates the microstructural phenomena involved in the temperature-dependent mechanical properties of the Premium rail steel through tensile tests at various temperatures. Dilatometry and scanning electron microscopy were used to characterize the materials before and after tensile tests at different temperatures. Finite element simulations were carried out to measure the residual stresses based on the experimental data acquired from the previous tests. Results show that the total elongation increases with the temperature, except for the elongation at 500 °C. Microstructural analysis near the fracture region reveals a more pronounced pearlitic contour at this temperature, indicating a mechanical strength reduction process. The fracture surface exhibits brittle cleavage fracture at 100 °C, while ductile fracture is observed at temperatures above 400 °C. Additionally, spheroidized microstructure is found near the fracture surface at 600 °C, suggesting the influence of deformation on the spheroidization process. Furthermore, the microstructure away from the fracture shows spheroidization initiation at 700 °C, indicating that severe plastic deformation considerably reduces the partial austenitization temperature and its consequent cementite spheroidization. These findings provide valuable insights into the temperature-dependent behavior of Premium rail steel, which can aid in its effective use in high-temperature applications.

**Keywords:** *rail steel, mechanical properties, thermal-dependent, welding metallurgy.*

## 1. Introduction

Rails are usually composed by different microstructures<sup>1-5</sup>. However, the heavy haul rails currently used in Brazil have pearlitic microstructure<sup>6-8</sup>. Moreover, the AREMA standard<sup>9</sup> does not allow the presence of acicular microconstituents in its composition, for instance, martensite and bainite. In this sense, a *Premium* rail type steel stands out from the other due to its higher hardness performance on heavy haul rails<sup>10-12</sup>.

The microstructure of the heat-affected zone (HAZ), resulted from the thermal cycle of rail welding, exhibits several distinct features. One of them includes a central region occasionally accompanied by pro-eutectoid ferrite due to decarburization during the flashing stage. Additionally, there are regions characterized by grain growth, grain refining, and spheroidization, occurring in the vicinity of the maximum inter-critical temperature where the divorced

eutectoid microconstituent undergoes transformation<sup>13</sup>. This region of spheroidization has a considerably lower hardness than the adjacent regions, which deforms more easily and can generate defects and subsequent failures during use<sup>14</sup>.

In this scenario, it is known that in the web region of the rail, there is a higher concentration of tensile residual stress<sup>15</sup> that can contribute to the horizontal split web type of failure<sup>16-18</sup>. This failure type starts in the rail web horizontally with the help of the residual stresses and propagates to branch and connect with the head and foot of the rail. Moreover, it is well-established that residual stresses present in the rail head can have an impact on the propagation of rolling contact fatigue (RCF) cracks<sup>19,20</sup>. As decreasing HAZ improves the mechanical performance and wear resistance of rail welds<sup>7,8,21,22</sup>, the distribution of residual stresses in railway rails has been studied intensively<sup>15</sup>.

Finite element simulation (FES) is a widely used tool for estimating residual stress values for complex geometries<sup>23,24</sup>. It is possible to estimate the distribution of

\*e-mail: joao.vitor@usp.br

Associate Editor: Aloisio Klein

Editor-in-Chief: Luiz Antonio Pessan

residual stresses in locations that are difficult to access from conventional testing, such as blind hole<sup>25,26</sup>, saw cut<sup>9</sup>, and X-ray diffraction<sup>27</sup>, where the latter penetrate minor into the material<sup>28</sup>. However, FES usually do not consider phase transformations, besides of the necessity input parameters usually unknown. When they regard the phase distribution, some studies observed the presence of martensite in places that, despite a higher propensity, very often do not occurs on the microstructure<sup>29,30</sup>. Furthermore, it has been identified that the temperature-dependent properties of the rail, mainly the physical properties, greatly influence the final value of the residual stresses and microstructure developed in the rail after welding<sup>31,32</sup>.

Several finite element simulations of rail welding rely on material parameters sourced from external references<sup>33-37</sup> or data extracted from software tools such as JMatPro®<sup>38,39</sup>. In both situations, the mechanical properties have not been observed through properly characterized tests, or the data has been taken from other references. Additionally, the microstructural results of the simulations were not conducted, and it was claimed that microstructures inconsistent with those observed were present.

In this sense, this work aims to predict through FES the temperature-dependent properties of a *Premium* rail based on simulation parameters obtained by mechanical tests and microstructural analysis. The incorporation of temperature-dependent mechanical properties will yield invaluable insights into the feasibility of employing rails in high-temperature environments, such as areas characterized by sharp curves, steep inclines, or fire hazards, contributing to assess the performance and reliability of rails under challenging thermal conditions.

## 2. Methodology

### 2.1. Material

A *Premium* rail steel with the chemical composition shown in Table 1 was used. The initial microstructure of the rail is completely pearlitic. The microstructure is shown in Figure 1 and more detailed characterization can be found in<sup>7,8,31,32</sup>. Despite the rail's chemical composition exhibiting a carbon equivalent higher than the eutectoid composition, the application of forced cooling heat treatment effectively prevented the formation of pro-eutectoid cementite in the base metal.

### 2.2. Microstructural characterization

Microstructural characterization was carried out on the longitudinal sections of the samples. The specimens were encapsulated in epoxy resin and carefully grinded until approximately half of the section. Subsequently, standard metallographic preparation was conducted, involving successive steps of grinding with SiC paper up to 1200 mesh, followed by polishing with diamond suspension with granulometry of up to 1 µm. The final polishing was carried out with 0.05 µm colloidal alumina solution. For etching, the samples were immersed in a 2% Nital solution (2% Nitric acid + 98% ethyl alcohol). Both fractures and the microstructure in the cross section close to the fractures

were obtained in a scanning electron microscope with field emission gun (SEM-FEG).

### 2.3. Tensile tests

The tensile tests were conducted in accordance with the ASTM E21-20 norm<sup>40</sup> in a Instron 2382 machine, utilizing cylindrical samples of 24mm in length and 4mm diameter at a wide range of temperatures (100 °C, 200 °C, 300 °C, 400 °C, 500 °C, 600 °C, 700 °C and 800 °C). Both heating and strain rate were kept constant, being 10 °C/min and 6mm/min, respectively.

### 2.4. Dilatometry

To measure the kinetics of the austenitization during the heating, one dilatometric test was performed in a Bähr Quenching Dilatometer DIL 805 L, using a cylindrical specimen with 10mm in length and 4mm in diameter tested under the conditions of the tensile experiments, i.e., using a heating rate of 10 °C/s until 800 °C had been reached.

The fraction of austenitization was calculated employing the leverage technique<sup>41,42</sup>. Two linear regressions were conducted, one before and another after the continuous cooling transformation. Equation 1 was utilized with the two straight lines obtained from the regressions to determine the percentage of austenite formed from pearlite during the heating process. The terms utilized in Equation 1 are described in Figure 2, which illustrates an example result obtained using a heating rate of 10 °C/s.

$$f_{pearlite} = \frac{P_2 - P'}{P_1 - P_2} \quad (1)$$

### 2.5. Finite element simulations

Utilizing the temperature-dependent mechanical properties obtained from the tensile tests, finite element simulation was conducted using the identical model construction methodology as outlined by Pereira et al.<sup>31,32</sup>. The simulation incorporated two distinct stages of thermal cycling: a heating stage and a subsequent cooling stage.

During the heating process, temperature-dependent properties were universally applied within the three-dimensional model limits of the rail. All temperature distributions and thermal stress accumulations generated during heating were recorded for the second stage. To achieve a maximum temperature of 1354 °C and a total heat-affected zone (HAZ) length of approximately 40 mm, sufficient heating energy and time were used as parameters. This maximum temperature of roughly 1354 °C was based on observations by Weingrill et al.<sup>39</sup>, which documented a flash-butt welding cycle measured by thermocouples. For the cooling step, a heat transfer coefficient (h) value of 25 W/m<sup>2</sup>K was used, as it closely approximates non-forced air cooling<sup>38</sup>.

The fraction of austenite was calculated by using the leverage technique, as explained before, and the other temperature-dependent physical and mechanical properties used were considered according to the phases and/or microconstituents present: austenite and pearlite. With the calculated lever rule described in Figure 2 and Equation 1, the temperature-dependent data presented in Table 2 were

used. The final property was a weighted average of the individual results with the phase/microconstituent fraction for each temperature.

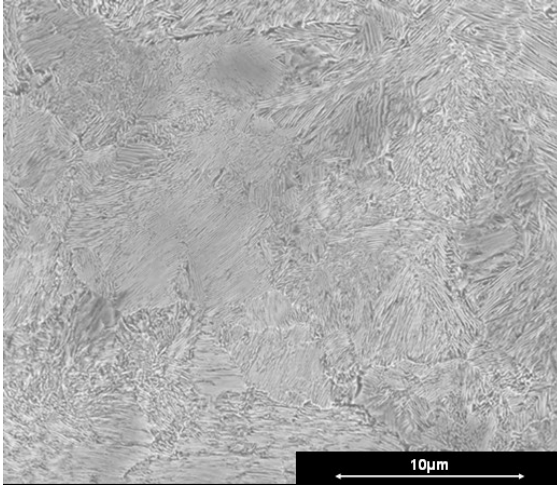


**Figure 1.** SEM-SE image of the original Premium rail steel microstructure consisting of a completely pearlitic microstructure.

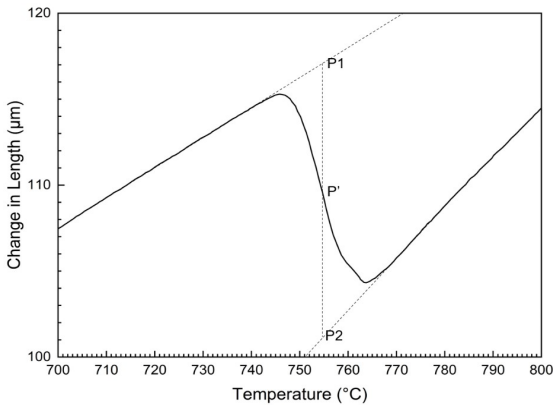


**Figure 2.** Example of actual heating and its dilatometric variation of the *Premium* rail at a rate of 10 °C/s. The lines from linear regression and the values given for realizing the lever rule (Equation 1) are also described.

### 3. Results

#### 3.1. High temperature mechanical properties and microstructures

The stress x strain curves obtained at high-temperatures are shown in Figure 3. It can be observed that the lower the tensile test temperature, the higher the ultimate tensile stress (UTS) and, generally, the lower the total elongation to failure. All conditions presented continuous yielding behavior. The value of  $\approx 1280$  MPa of UTS was achieved for the sample tensile tested at 100 °C, decreasing to  $\approx 1080$  MPa at 400 °C and  $\approx 880$  MPa at 500 °C. Tensile tests at higher temperature induced a higher drop in the UTS values, achieving  $\approx 520$  MPa at 600 °C, and strong dropping to  $\approx 200$  MPa and  $\approx 80$  MPa for tests carried out at 700 °C and 800 °C, respectively.

A comparison of the  $\sigma_{0.2}$ , UTS, and Young's modulus is depicted in Figure 4. The results show that the higher the tensile test temperature, the lower the yield strength value, UTS and Young's modulus value. The Young's modulus drops from  $\approx 192$  GPa when tested at 100 °C to  $\approx 164$  GPa to a test carried out at 400 °C, followed by a linear drop up to  $\approx 104$  GPa at 700 °C. On a similar behavior, the Yield strength slight drops from testing at 100 °C to 500 °C, afterwards it presents

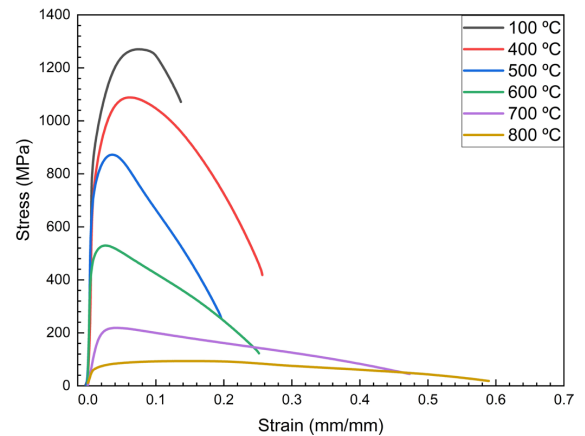


**Figure 3.** High-temperature tensile tests curves (stress X strain) from the Premium rail steel.

**Table 1.** Chemical composition (wt.%) of the Premium rail steel.

C	Si	Mn	P	S	Cr	Ni	Mo	Ti	C <sub>eq</sub>
0.81	0.23	1.03	0.01	0.01	0.22	0.01	0.02	0.002	1.07

**Table 2.** Temperature-dependent physical properties of austenite and pearlite<sup>24,43-45</sup>.

Microconstituent	Thermal conductivity (W/[m·°C])	Heat capacity (J/[kg·°C])
Austenite	$-6 \cdot 10^{-9}T^3 + 9 \cdot 10^{-6}T^2 + 8 \cdot 10^{-3}T + 15$	$-4 \cdot 10^{-8}T^3 + 4 \cdot 10^{-5}T^2 + 9 \cdot 10^{-2}T + 532$
Pearlite	$-1 \cdot 10^{-9}T^3 - 2 \cdot 10^{-6}T^2 - 2 \cdot 10^{-2}T + 49$	$5 \cdot 10^{-8}T^3 \cdot 10^{-5}T^2 + 0.3T + 484$

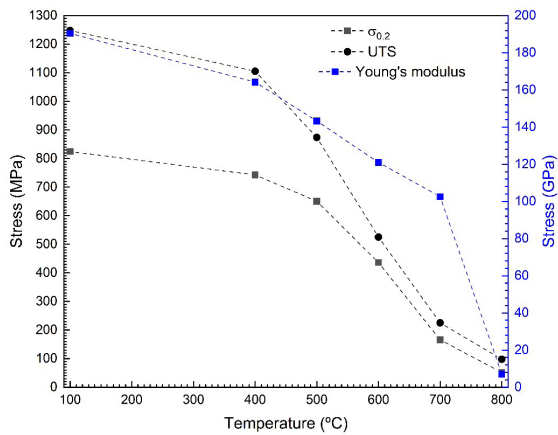


**Figure 4.** Yield strength and ultimate tensile stress from the high-temperature tensile tests of the Premium rail steel.

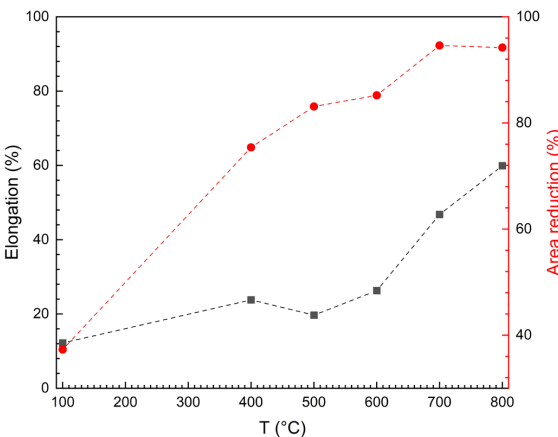


**Figure 5.** Total elongation (%) and area reduction (%) of the high temperature tensile tests.

a strong decrease from  $\approx 650$  MPa at 500 °C to 420, 180 and 50 MPa for testing at 600, 700, and 800 °C, respectively.

The results of the high-temperature tensile test, including total elongation (%) and area reduction, are presented in Figure 5. The area reduction demonstrated a direct correlation with the test temperature, steadily increasing until reaching 700 °C, after which it stabilized compared to the tests conducted at 800 °C. Interestingly, the elongation did not follow a logical pattern, as the test performed at 500 °C exhibited a lower value than the one conducted at 400 °C. However, it is worth noting that the area reduction at 500 °C was greater than that at 400 °C

The final appearance of the tensile tested specimens is shown in Figure 6. The specimen tested at 100 °C shows a bright and clean surface, very similar to the original color of the room-hardened steel. The sample subjected to the test at 400 °C exhibits a distinct bluish coloration on its surface. This bluish tint is due to oxidation at this temperature<sup>46</sup>. From 500 °C up to higher temperatures, the specimen's surface shows a darker feature due to the surface oxidation during the tests. All specimens showed plastic deformation, but as seen in Figure 3, the higher the test temperature, the greater this deformation is.

The SEM images of the tensile tested sample's fracture are depicted in Figure 7. As expected, the fracture surface of the test performed at 100 °C shows mixed ductile and brittle aspects but with a higher amount of cleavage fracture mechanism. At 400 °C, the surface shows more ductile micro-mechanism of dimple formation and, although most of the surface shows dimples with a smaller dimension, some craters with considerable larger sizes are observed. These craters have a surface texture considerably smoother than a dimple. The sample tested at 500 °C shows a fracture surface predominantly with dimples but with a coarser morphology than the tests performed at 400 °C and 600 °C. The fracture surface of the specimen tested at 800 °C shows that an almost perfect plastic deformation occurred, presenting a very small final resistant section.



**Figure 6.** Specimens after the high temperature tensile tests of the Premium rail steel.



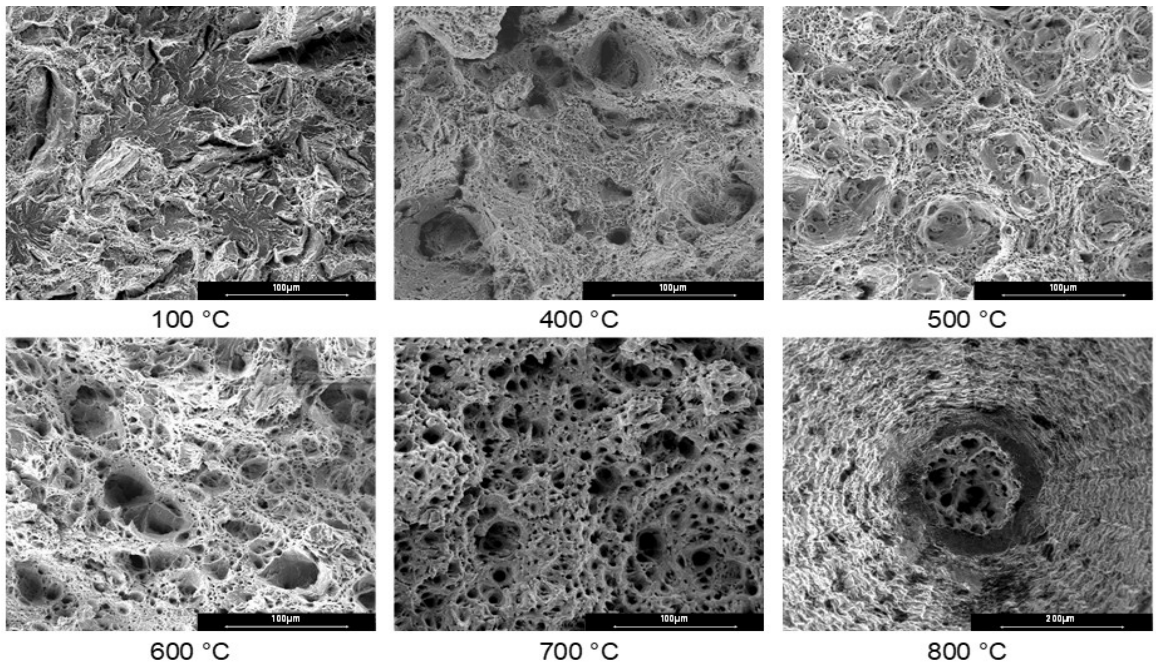


**Figure 7.** SEM images of the fracture surface of the specimens from the high-temperature tensile test.

Microstructure aspects close to the tensile test fracture, in the cross-section plane, are shown in Figure 8. At 100 °C, the microstructure showed little microstructural change, i.e., the pearlite lamellae are not aligned in the deformation direction, similar to the micrograph presented in Figure 1. The microstructure of the test performed at 400 °C shows a considerable change: the pearlite lamellae are aligned in the direction of deformation. At 500 °C, the microstructure showed a pearlite lamellae alignment but also showed the presence of cementite in the pearlitic colony contours. The microstructures of the tests performed at 600 °C and 700 °C presented a cementite spheroidization. At 800 °C, the microstructure of the specimen was utterly pearlitic with an oxide-covered surface, which is in agreement with the surface presented in Figure 7.

## 4. Discussion

### 4.1. Mechanical properties and microstructural features

The high-temperature tensile test results indicate that as the temperature increases, both the yield strength and ultimate tensile strength (UTS) decrease, while total elongation increases. These findings are consistent with reports on the temperature-dependent mechanical properties of similar steel types<sup>29,30</sup>. Specifically, the decrease in yield strength follows the same trend observed by Ma et al.<sup>30</sup> and Cal et al.<sup>29</sup>. However, the initial yield strength in this study, shown in Figure 4, is higher than that reported by Ma et al.<sup>30</sup> and Cal et al.<sup>29</sup>, likely due to the material being a Premium class rail. Additionally, the Young's modulus of the material exhibited an almost linear decline with rising temperature, ultimately decreasing by approximately 50%.

The total elongation decreases at 500 °C and 600 °C, contradicting the logic that the higher the temperature, the higher the elongation (Figure 5), occurs due to cementite formation around pearlitic colonies (Figure 8). This cementite leads to the embrittlement, decreasing the total elongation. Such effect may be related to the larger dimple craters observed in the fractography of the specimen tested at 500 °C (Figure 7). These craters with larger diameters at shallower depths have smoother surfaces and may be related to the cementite layer observed in Figure 8.

Bauri et al.<sup>8</sup> observed a fracture in a tensile test in the unsoftened region of the flash-butt welded rail. According to the authors, at the cross-section, a higher amount of cementite at grain boundaries than in the adjacent areas was observed. Although the flash-butt process welding inserts deformation by compression, we can infer that this region presented a higher amount of cementite on the grain boundary of the pearlitic colony observed by Bauri et al.<sup>8</sup> presented a thermal cycle with a maximum temperature of approximately 500 °C. The drop in mechanical properties in the thermal cycling region, with an estimated maximum temperature of 500 °C, suggests that an embrittlement effect may have occurred, as indicated by the decrease in elongation shown in Figure 5.

Another interesting aspect observed in Figure 8 was that, in the test performed at 600 °C, a microstructure spheroidization occurs in the region near the fracture. This spheroidization occurred at a considerably lower temperature than commonly observed for non-deformed rail steels<sup>13</sup>. Nevertheless, it can be explained by the austenitization kinetics increase, which depends on the microstructure thinning<sup>47-49</sup>. During plastic deformation, the alignment and refinement of the pearlite interlamellar distance and the pearlitic colony contour flattening increase the austenitic

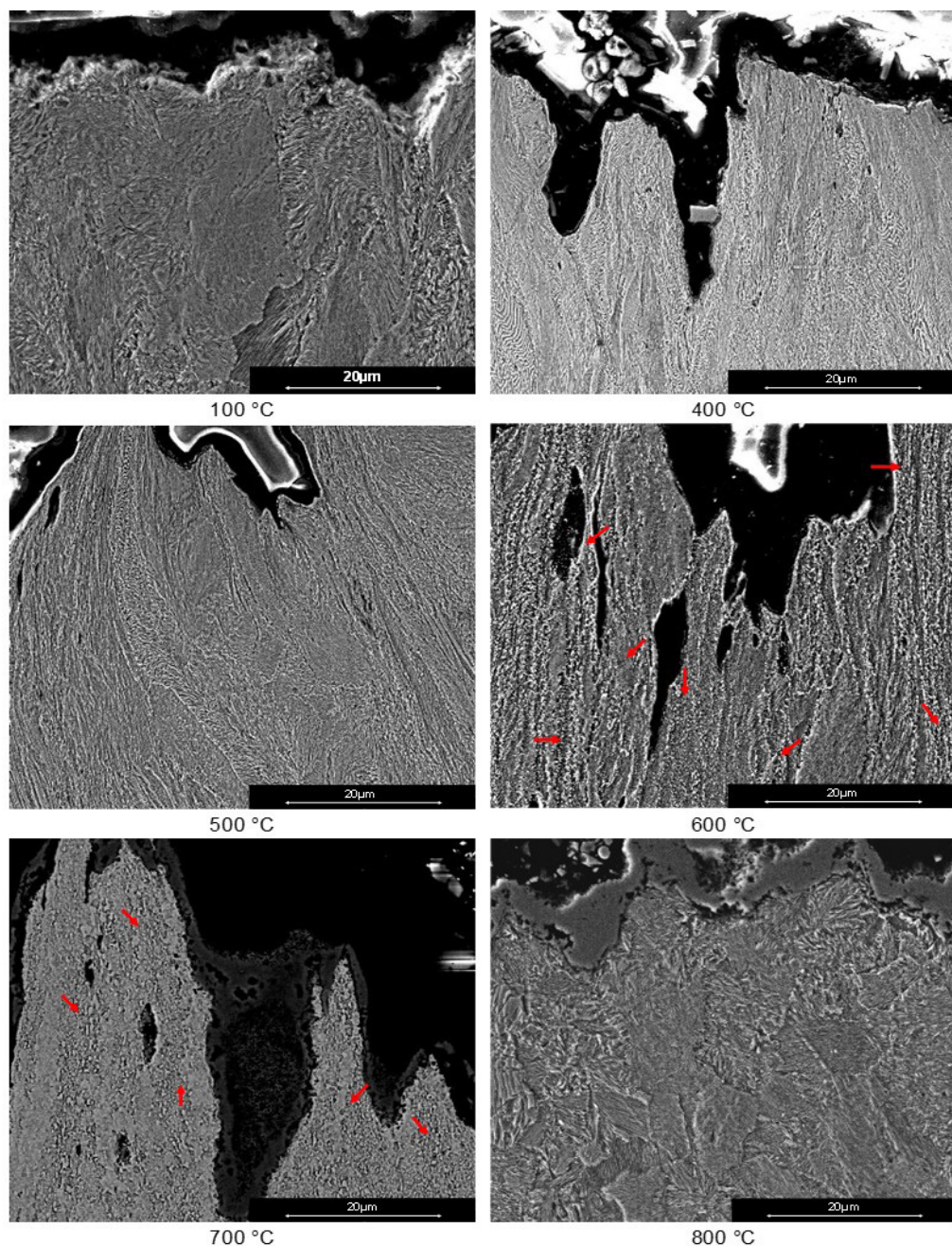


**Figure 8.** Microstructure of the cross section near the fracture of high-temperature tensile test specimens. SEM-SE, etching by immersion in Nital 2% solution for 30s. The red arrows on the images of 600 °C and 700 °C shows regions of spheroidization.

transformation kinetics, enabling a partial transformation and consequent spheroidization of the remaining cementite<sup>50</sup>. The deformation at high temperatures favors the creation of new dislocations, decreasing pearlitic lamellae distances, and the formation of new sub-boundaries. Thus, accumulating a considerable amount of strain and surface energy and significantly increasing austenite nucleation sites<sup>50-52</sup>.

Figure 9 illustrates the microstructure of the same tensile specimen located far from the point of fracture, yet still subjected to tensile stress. At 400 °C, the alignment of

cementite lamellae and the flattening contours of the pearlitic colony are not observable. Similarly, the spheroidization of cementite, as depicted in Figure 8, is not evident at 600 °C. Thus, it becomes apparent that spheroidization is greatly influenced by plastic deformation, leading to a decrease in the spheroidization temperature. The impact of strain on spheroidization has been discussed by Chojnowski and Tegart<sup>53</sup> and Bruns and Kaspar<sup>54</sup>. When the temperature is set at 700 °C, it can be observed that a lower applied strain, combined with elevated temperature, promotes



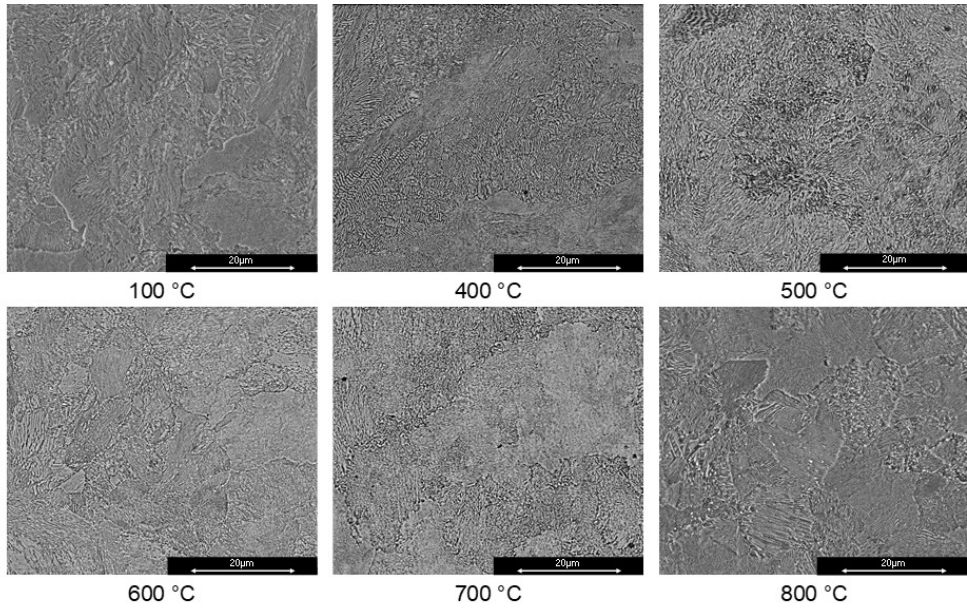


**Figure 9.** Microstructure away from fracture of high-temperature tensile test specimens. SEM-SE, etching by immersion in Nital 2% solution for 30 s.

partial spheroidization, particularly along the contour of the pearlitic colony. Furthermore, it is noteworthy that spheroidization at 700 °C is considerably less pronounced compared to the region closer to the fracture. As for the 800 °C temperature, both near and far from the fracture, a fully pearlitic microstructure is evident, but a small fraction of spheroidized cementite is present in the far region from the fracture. At this temperature, complete austenitization occurs, and pearlitic transformation transpires during cooling. The presence of small spheres in the region distant from the fracture indicates that minimal deformation leads to almost complete austenitization, with some carbides retaining their spherical form. However, it is important to note that during the subsequent cooling process and with the specific cooling rate employed, the pearlitic transformation occurs. This transformative phenomenon has been extensively discussed and documented by Ankit et al.<sup>55</sup>, providing further insights into the mechanism and behavior of pearlitic transformation under similar conditions.

Finally, the observed decrease in mechanical properties, particularly yield strength and ultimate tensile strength, along with changes in total elongation, highlights the significant impact of temperature on the material's behavior. The formation of cementite and the resultant embrittlement at specific temperatures further emphasize the complexity of these effects. These insights lay a crucial foundation for understanding the thermal and mechanical responses of the rail material. Transitioning to the next phase of the analysis, the discussion will now delve into the simulations to further explore and validate these experimental observations. By integrating computational models, the study aims to provide a comprehensive understanding of the thermal and mechanical behavior under varying conditions, offering deeper insights

into the material's performance and potential improvements in rail manufacturing and maintenance processes.

#### 4.2. Residual stress simulation analysis

With the data obtained from the hot tests and phase transformation data together with the physical properties data as a function of temperature, it was possible to carry out simulations using the finite element method with real data calculated.

The finite element method simulation of the residual stresses in the vertical direction (y-direction - S22) are shown in Figure 10. Following the distance from the welded face, the rail passes through a region containing compressive stress (blue part) after the tensile area. The highest tensile stress in the vertical direction is located in the central area of the web (red part), where the maximum value is slightly away from the welded surface. However, the maximum value was 552 MPa, while the minimum was -392 MPa.

The result of the residual stress distribution in the longitudinal direction (z-axis - S33) is shown in Figure 11. A more significant amount of compressive stress is observed mainly in the central region of the web. A small amount of compressive stress is kept in the rail head region, followed by a slight tensile stress. The maximum stress value was 253 MPa, while the minimum was -118 MPa.

The centerline residual stress in the vertical direction (y-axis, S22) at the center of the rail web, both at the surface and the core of the rail, and extending longitudinally away from the welded face, is illustrated in Figure 12a. The distributions exhibit symmetry, but the depths at which they intersect vary. This indicates a complex interaction of thermal and mechanical stresses during the welding process, affecting different layers of the rail. Figure 12b depicts the centerline residual stress in the longitudinal direction (z-axis, S3) at both the middle and corner of the rail head surface,

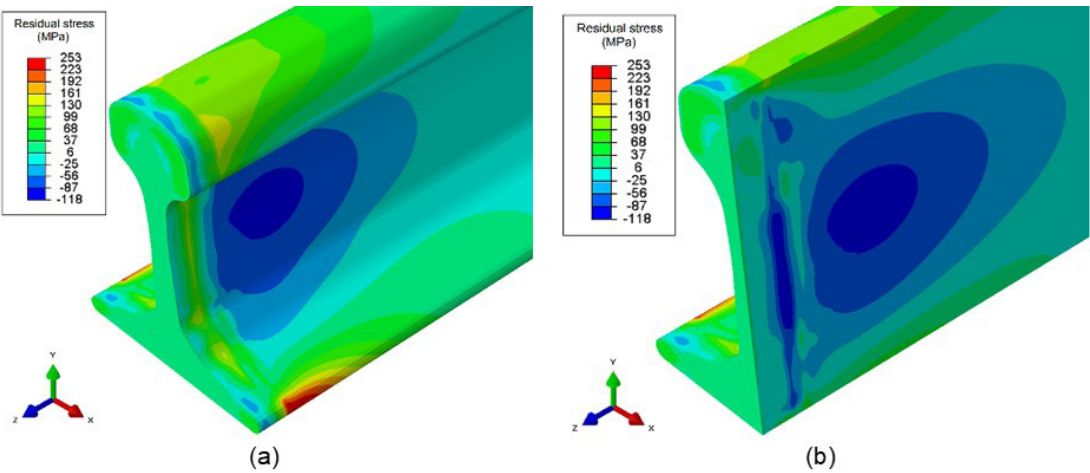


**Figure 10.** S22 residual stress distribution simulation with the parameters set to achieve HAZ size of 45 mm and a heat transfer coefficient of 25 W/m<sup>2</sup>K. (a) represents the result observed on the surface, and (b) represents the result observed in the central region of the rail.

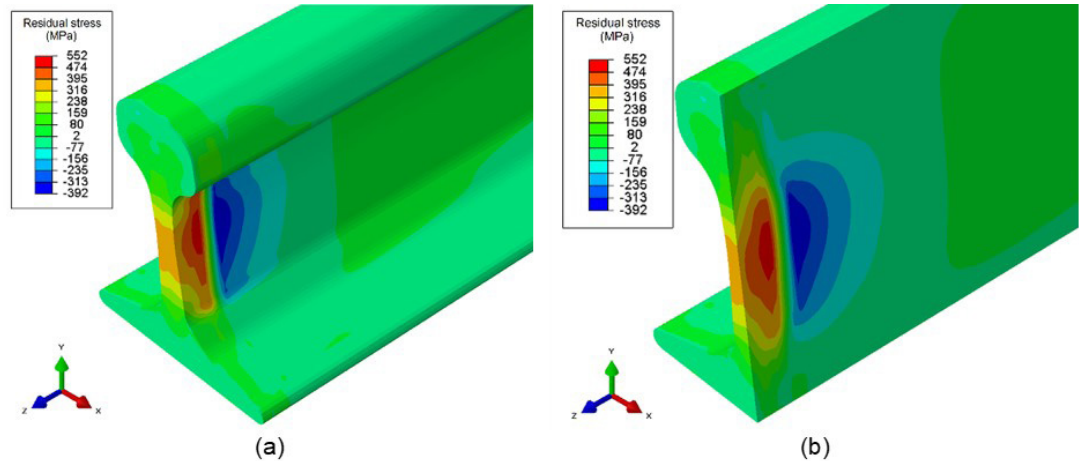


**Figure 11.** S33 residual stress distribution simulation with the parameters set to achieve HAZ size of 45 mm and a heat transfer coefficient of 25 W/m<sup>2</sup>K. (a) represents the result observed on the surface, and (b) represents the result observed in the central region of the rail.

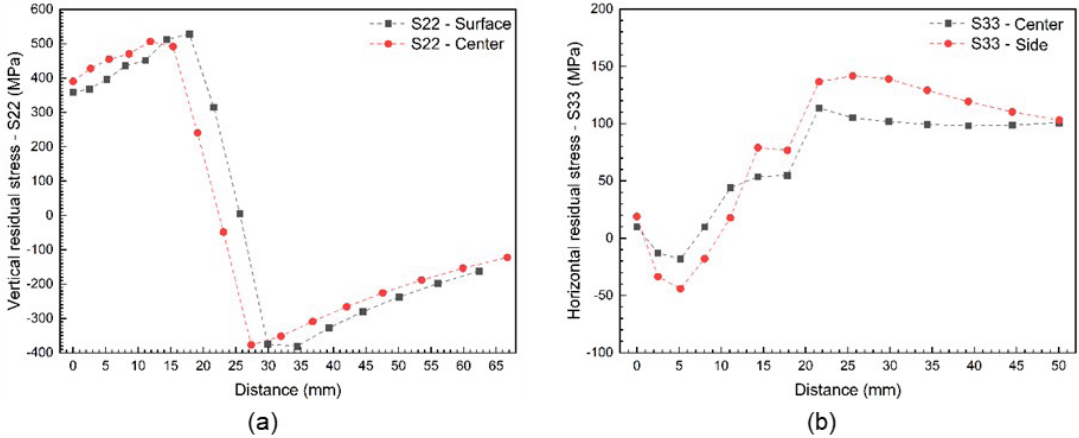


**Figure 12.** Residual stress profile distributed in the longitudinal direction from the welded face. (a) Residual stress in the vertical direction (y-axis - S22) in the central region and on the middle surface of the rail core. (b) Residual stress in the longitudinal direction (z-axis - S33) in the center and on the side of the rail head.



also extending longitudinally from the welded face. This figure compares two stress lines on the surface: one at the center of the rail head in straight rail sections and the other at the side of the rail head in curved rail sections. These regions are critical as they correspond to the contact areas with the wheel, which experience significant stress during operation. The depth distance between the two curves is not shown in the figure because a detailed analysis is required to understand the differences between the surface and the core stress distributions.

According to Figure 11, there is a higher concentration of tensile stress in the web region of the rail. Haibatollahi and Tehrani<sup>37</sup>, in their simulations, also observed tensile stress in the web, which transitioned into compressive stress at a slightly distant region from the bonding area, located at the center of the weld. Compared to the results of Oliveira et al.<sup>15</sup>, the maximum residual stresses of the simulation observed in Figure 11 were considerably lower than the measured ones. Oliveira et al.<sup>15</sup> observed that the longitudinal stresses at the rail head profile were approximately 350 MPa. In contrast, the maximum longitudinal stress observed at the corner of the rail head showed a maximum value of around 200 MPa, close to that observed in Figure 12, but with a slightly different distribution than that observed by Oliveira et al.<sup>15</sup>.

The distribution of vertical residual stresses in the rail web exhibited both similar distribution and values to those observed by Oliveira et al.<sup>15</sup>. In their study, they reported a maximum value of approximately 350 MPa, whereas the simulation presented in Figure 10 showed a slightly higher value of 552 MPa. It is worth noting that further refinement of the model can be achieved by incorporating a module that offers greater precision in representing phase transformations. Nonetheless, by utilizing the temperature-dependent mechanical properties data, a significant convergence between the observed values from observed data of Oliveira et al.<sup>15</sup> and distribution was achieved, indicating a notable approximation.

Furthermore, X-ray diffraction analysis has a shallow depth, in the range of a few microns<sup>28,56</sup>. Thus, the residual stress observed by Oliveira et al.<sup>15</sup> is superficial. Compared with the analysis at the rail web surface in Figure 10a, it is noted that the vertical tensile stress is with a maximum of approximately 400 MPa, very close to the value observed by Oliveira et al.<sup>15</sup>.

## 5. Conclusions

Tensile tests were conducted on premium pearlitic rails at various temperatures, leading to the following conclusions:

- The yield strength, ultimate tensile strength (UTS), and Young's modulus exhibited a decrease with increasing temperature. The yield strength and UTS demonstrated a higher rate of reduction within the temperature range of 400 °C to 700 °C. The reduction in Young's modulus followed an approximately linear trend.
- The total elongation and area reduction displayed a direct relationship with temperature, meaning that higher temperatures resulted in higher values, except for the elongation at 500 °C.
- The fracture surface exhibited a combination of cleavage and dimples in the test conducted at

100 °C, while pure ductile behavior with dimples was observed at all other temperatures. At 800 °C, yielding occurred until there was virtually no resistance area left during yielding.

- Pro-eutectoid cementite was detected in the microstructure near the fracture site of the specimen tested at 500 °C.
- Spheroidization of cementite was also observed in the region close to the fracture at 600 °C. This indicates that the influence of strain or tension contributed to the spheroidization process of cementite.
- The use of the temperature-dependent physical and mechanical properties collected by the tensile tests as inputs on finite element simulations were successful, as the results predicted accurately the stresses caused by the HAZ in the rail weld, both their values and their distribution.

## 6. Acknowledgments

The authors would like to thank the LTF laboratory and the project “*Cátedra de contato entre Roda&Trilho*” of VALE S.A. The authors acknowledge the financial support provided by CAPES (process number: 88887.461594/2019-00).

## 7. References

1. Masoumi M, Echeverri EAA, Tschiptschin AP, Goldenstein H. Improvement of wear resistance in a pearlitic rail steel via quenching and partitioning processing. *Sci Rep*. 2019;9(1):7454. <http://doi.org/10.1038/s41598-019-43623-7>.
2. Masoumi M, Tressia G, Centeno DMA, Goldenstein H. Improving the mechanical properties and wear resistance of a commercial pearlitic rail steel using a two-step heat treatment. *Metall Mater Trans, A Phys Metall Mater Sci*. 2021;52(11):4888-906. <http://doi.org/10.1007/s11661-021-06432-0>.
3. Yates JK. Innovation in rail steel. *Sci Parliam*. 1996;53(2-3):13.
4. Bhadeshia HKDH, Jerath V. Relating to carbide-free bainitic steels and method of producing such steels. United States patent US 5879474A. 1999, Mar 09.
5. Bhadeshia HKDH. Novel steels for rails. In: Jürgen Buschow KH, Cahn RW, Flemings MC, Ilshner B, Kramer EJ, Mahajan S, et al., editors. *Encyclopedia of materials: science and technology*. New York: Elsevier; 2002. p. 1-7.
6. Porcaro RR, Lima DAP, Faria GL, Godefroid LB, Cândido LC. Microestrutura e propriedades mecânicas de um aço para trilhos ferroviários soldado por centelhamento. *Soldag Insp*. 2017;22(1):59-71. <http://doi.org/10.1590/0104-9224/si2201.07>.
7. Alves LHD, Lagares ML, Moreira RM Fo, Tepedino T, Goldenstein H. Predictive mathematical modeling of the flash-butt welding process to optimize the properties of welds of premium and super premium rails. *Narvik: IHHA*; 2019.
8. Bauri LF, Alves LHD, Pereira HB, Tschiptschin AP, Goldenstein H. The role of welding parameters on the control of the microstructure and mechanical properties of rails welded using FBW. *J Mater Res Technol*. 2020;9(4):8058-73. <http://doi.org/10.1016/j.jmrt.2020.05.030>.
9. AREMA: American Railway Engineering and Maintenance-of-Way Association. *Manual for railway engineering*. Lanham, MD: AREMA; 2010. Chapter 4, Rail.
10. Hu Y, Zhou L, Ding HH, Lewis R, Liu QY, Guo J, et al. Microstructure evolution of railway pearlitic wheel steels under rolling-sliding contact loading. *Tribol Int*. 2021;154:106685. <http://doi.org/10.1016/j.triboint.2020.106685>.

11. Girsch G, Keichel J, Gehrmann R, Zlatnik A, Frank N. Advanced rail steels for heavy haul application-track performance and weldability. In: 9th International Heavy Haul Conference; 2009; Shanghai, China. Proceedings. Shanghai: China Railway Publishing House; 2009. p. 171-8. <http://doi.org/10.1371/journal.pone.0161382>.
12. Micheletto A, Cookson J, Pang Y, Chen B, Mutton P. The structural integrity of flash-butt welded premium rail steel: evaluation of strength, microstructure and defects. *Proc Inst Mech Eng, F J Rail Rapid Transit*. 2021;235(8):1006-12. <http://doi.org/10.1177/0954409720973138>.
13. Nishikawa LP, Goldenstein H. Divorced eutectoid on heat-affected zone of welded pearlitic rails. *J Miner Met Mater Soc*. 2019;71(2):815-23. <http://doi.org/10.1007/s11837-018-3213-5>.
14. Mutton P, Cookson J, Qiu C, Welsby D. Microstructural characterisation of rolling contact fatigue damage in flashbutt welds. *Wear*. 2016;366-367:368-77. <http://doi.org/10.1016/j.wear.2016.03.020>.
15. Oliveira BS, Rodrigues LAS, Costa ES, Braga EM, Reis MAL. X-ray diffraction analysis of residual stresses in the premium rails welded by flash butt process. *Soldag Insp*. 2020;25:e2529. <http://doi.org/10.1590/0104-9224/si25.29>.
16. Ito HL, Gomes JDC. Análise de falhas: um dever do IPT. *IPT Tecnol Inov*. 2019;3:35-64.
17. Godefroid LB, Faria GL, Cândido LC, Viana TG. Fatigue failure of a flash butt welded rail. *Procedia Mater Sci*. 2014;3:1896-901. <http://doi.org/10.1016/j.mspro.2014.06.306>.
18. Mousavizade M, Farhangi H. Characterization of surface defects associated with flash butt-welded pearlitic rails and their contribution to overload and fatigue failures. *Adv Mat Res*. 2010;83-86:1262-9. <http://doi.org/10.4028/www.scientific.net/AMR.83-86.1262>.
19. Deng TS, Zhao X, Wu B, Li W, Wen ZF, Jin XS. Prediction of crack initiation of rail rolling contact fatigue. *Appl Mech Mater*. 2013;344:75-82. <http://doi.org/10.4028/www.scientific.net/AMM.344.75>.
20. Steenberg M. Rolling contact fatigue in relation to rail grinding. *Wear*. 2016;356-357:110-21. <http://doi.org/10.1016/j.wear.2016.03.015>.
21. Saita K, Ueda M, Miyazaki T. Developing technologies to improve the reliability of flash-butt welds. In: 11th International Heavy Haul Association Conference (IHHA); 2017; Cape Town, South Africa. Proceedings. Red Hook: IHHA; 2017. p. 208-15.
22. Pang Y, Grilli N, Su H, Liu W, Ma J, Yu SF. Experimental investigation on microstructures and mechanical properties of PG4 flash-butt rail welds. *Eng Fail Anal*. 2022;141:106650. <http://doi.org/10.1016/j.engfailanal.2022.106650>.
23. Simulia. Abaqus 6.13: CAE user's guide. Vélizy-Villacoublay, France: Dassault Systèmes; 2013.
24. Ariza EA, Martorano MA, Lima NB, Tschiptschin AP. Numerical simulation with thorough experimental validation to predict the build-up of residual stresses during quenching of carbon and low-alloy steels. *ISIJ Int*. 2014;54(6):1396-405. <http://doi.org/10.2355/isijinternational.54.1396>.
25. ASTM: American Society for Testing and Materials. ASTM E837: determining residual stresses by the hole-drilling strain-gage method. West Conshohocken: ASTM; 2013. <http://doi.org/10.1520/E0837-20>.
26. Schajer GS, Whitehead PS. Hole drilling and ring coring. In: Schajer GS, editor. *Practical residual stress measurement methods*. Chichester: John Wiley & Sons; 2013. p. 29-64. <http://doi.org/10.1002/9781118402832.ch2>.
27. Murray CE, Noyan IC. Applied and residual stress determination using X-ray diffraction. In: Schajer GS, editor. *Practical residual stress measurement methods*. Chichester: John Wiley & Sons; 2013. <http://doi.org/10.1002/9781118402832.ch6>.
28. Cullity BD. *Elements of X-ray diffraction*. 2nd ed. Reading, MA: Addison-Wesley Publishing; 1978.
29. Cal Z, Nawafune M, Ma N, Qu Y, Cao B, Murakawa H. Residual stresses in flash butt welded rail. *Trans JWRI*. 2011;40:79-87.
30. Ma N, Cai Z, Huang H, Deng D, Murakawa H, Pan J. Investigation of welding residual stress in flash-butt joint of U71Mn rail steel by numerical simulation and experiment. *Mater Des*. 2015;88:1296-309. <http://doi.org/10.1016/j.matdes.2015.08.124>.
31. Pereira HB, Echeverri EAA, Alves LHD, Goldenstein H. Influência das propriedades mecânicas e físicas dependentes da temperatura nas tensões residuais por simulação de soldagem de trilhos por Flash-Butt. In: *V Simpósio de Engenharia Ferroviária*; 2022. Anais. Campinas: Galoá Ciência; 2022. <http://doi.org/10.17648/sef-2022-146919>.
32. Pereira HB, Anderson E, Echeverri A, Henrique L, Alves D, Goldenstein H. Evaluation of the effect of heat input and cooling rate of rail flash-butt welding using finite element method simulation. *Soldag Insp*. 2022;27:1-18. <http://doi.org/10.1590/0104-9224/si27.01>.
33. Porcero RR, Araújo FC, Godefroid LB, Faria GL, Silva LL, Leite L. Simulação do processo de soldagem elétrica por centelhamento de um aço para trilhos ferroviários. Parte 2: análise dilatométrica e numérica. *Soldag Insp*. 2020;25:1-11. <http://doi.org/10.1590/0104-9224/si25.33>.
34. Tawfik D, Mutton PJ, Chiu WK. Transient thermal stress analysis on rapid post-weld heat treatments applied to flash butt welded rails. *Sci Technol Weld Join*. 2006;11(3):326-36. <http://doi.org/10.1179/174329306X107629>.
35. Tawfik D, Mutton PJ, Chiu WK. Experimental and numerical investigations: alleviating tensile residual stresses in flash-butt welds by localised rapid post-weld heat treatment. *J Mater Process Technol*. 2008;196(1-3):279-91. <http://doi.org/10.1016/j.jmatprotec.2007.05.055>.
36. Tawfik D, Mutton PJ, Chiu WK. Modifying residual stress levels in rail flash-butt welds using localised rapid post-weld heat treatment and accelerated cooling. *Int Heat Treat Surf Eng*. 2009;2(3-4):126-30. <http://doi.org/10.1179/174951508X429212>.
37. Haibatollahi SP, Tehrani PH. Prediction of residual stress distribution in flash butt welded rails using electro-thermo-mechanical simulation. *Int J Veh Struct Syst*. 2013;5(2):53-7. <http://doi.org/10.4273/ijvss.5.2.02>.
38. Weingrill L, Nasiri MB, Enzinger N. Thermo-metallurgically coupled numerical simulation and validation of multi-layer gas metal arc welding of high strength pearlitic rails. *Weld World*. 2019;63(1):63-73. <http://doi.org/10.1007/s40194-018-0639-x>.
39. Weingrill L, Krutzler J, Enzinger N. Temperature field evolution during flash butt welding of railway rails. *Mater Sci Forum*. 2016;879:2088-93. <http://doi.org/10.4028/www.scientific.net/MSF.879.2088>.
40. ASTM: American Society for Testing and Materials. ASTM E21-20: test methods for elevated temperature tension tests of metallic materials. West Conshohocken: ASTM; 2020. <http://doi.org/10.1520/E0021-20>.
41. Cezário ALS, Faria GL. Proposition of an empirical functional equation to predict the kinetics of austenite to ferrite transformation in a continuous cooled IF-Ti-stabilized steel. *Mater Res*. 2021;24(2):1-10. <http://doi.org/10.1590/1980-5373-mr-2020-0498>.
42. Rodrigues KF, Faria GL. Characterization and prediction of continuous cooling transformations in rail steels. *Mater Res*. 2021;24(5):e20200519. <http://doi.org/10.1590/1980-5373-mr-2020-0519>.
43. Bhadeshia HKDH. Material factors. In: *ASM International, editor. Handbook of residual stress and deformation of steel*. Materials Park: ASM International; 2022.
44. Schröder R. Influences on development of thermal and residual stresses in quenched steel cylinders of different dimensions.

- Mater Sci Technol. 1985;1(10):754-64. <http://doi.org/10.1179/mst.1985.1.10.754>.
45. Pietzsch R, Brzoza M, Kaymak Y, Specht E, Bertram A. Simulation of the distortion of long steel profiles during cooling. *J Appl Mech*. 2007;74(3):427-37. <http://doi.org/10.1115/1.2338050>.
  46. Vander Voort GF. Embrittlement of steels. Section: service characteristics of carbon and low-alloy steels. In: ASM International, editor. *Properties and selection: irons, steels, and high performance alloys*. Materials Park: ASM International; 2005. p. 1058-133. (vol. 1).
  47. Speich GR, Szirmai A, Richards MJ. Formation of austenite from ferrite and ferrite-carbide aggregates. *Trans Metall Soc AIME*. 1969;245:1063.
  48. Mehl RF. The structure and rate of formation of pearlite. *Metallogr. Microstruct. Anal*. 1941;4(5):423-43. <http://doi.org/10.1007/s13632-015-0226-0>.
  49. Roósz A, Gácsi Z, Fuchs EG. Isothermal Formation of Austenite in Eutectoid Plain Carbon Steel. *Acta Metall*. 1983;31(4):509-17. [http://doi.org/10.1016/0001-6160\(83\)90039-1](http://doi.org/10.1016/0001-6160(83)90039-1).
  50. Oliveira MAF, Jorge AM Jr, Balancin O. Influence of deformation on the kinetics of phase transformation in a forging steel during warm working. *Mater Res*. 2004;7(2):247-53. <http://doi.org/10.1590/S1516-14392004000200006>.
  51. Liu X, Solberg JK, Gjengedal R. Influence of multipass deformation on Ar 3 for niobium bearing steel using torsion simulations. *Mater Sci Technol*. 1996;12(4):345-50. <http://doi.org/10.1179/mst.1996.12.4.345>.
  52. Niikura M, Fujioka M, Adachi Y, Matsukura A, Yokota T, Shirota Y, et al. New concepts for ultra refinement of grain size in Super Metal Project. *J Mater Process Technol*. 2001;117(3):341-6. [http://doi.org/10.1016/S0924-0136\(01\)00800-7](http://doi.org/10.1016/S0924-0136(01)00800-7).
  53. Chojnowski EA, Tegart WJ. Accelerated spheroidization of pearlite. *Met Sci J*. 1968;2(1):14-8. <http://doi.org/10.1179/030634568790443585>.
  54. Bruns H, Kaspar R. Pearlite spheroidization by thermomechanical treatment of directly charged thin slabs. *Steel Res*. 1997;68(4):158-62. <http://doi.org/10.1002/srin.199700557>.
  55. Ankit K, Mukherjee R, Nestler B. Deviations from cooperative growth mode during eutectoid transformation: mechanisms of polycrystalline eutectoid evolution in Fe-C steels. *Acta Mater*. 2015;97:316-24. <http://doi.org/10.1016/j.actamat.2015.06.050>.
  56. Schajer GS, Ruud CO. Overview of residual stresses and their measurement. In: Schajer GS, editor. *Practical residual stress measurement methods*. Chichester: John Wiley & Sons; 2013. p. 1-28. <http://doi.org/10.1002/9781118402832.ch1>.

### Data Availability

The dataset supporting the results of the study is not publicly available.